CHAPTER 11
RADAR CROSS SECTION

Eugene F. Knott
The Boeing Company

11.1 INTRODUCTION

A radar detects or tracks a target, and sometimes can identify it, only because there is an echo signal. It is therefore critical in the design and operation of radars to be able to quantify or otherwise describe the echo, especially in terms of such target characteristics as size, shape, and orientation. For that purpose the target is ascribed an effective area called the *radar cross section*. It is the projected area of a metal sphere which would return the same echo signal as the target had the sphere been substituted for the target.

Unlike the echo of the sphere, however, which is independent of the viewing angle, the echoes of all but the simplest targets vary significantly with orientation. As such, one must mentally allow the size of this fictitious sphere to vary as the aspect angle of the target changes. As will be shown, the variation can be quite rapid, especially for targets many wavelengths in size.

The echo characteristics depend in strong measure on the size and nature of the target surfaces exposed to the radar beam. The variation is small for electrically small targets (targets less than a wavelength in size) because the incident wavelength is too long to resolve target details. On the other hand, the flat, singly curved and doubly curved surfaces of electrically large targets each give rise to different echo characteristics. Reentrant structures like jet engine intakes and exhausts generally have large echoes, and even the trailing edges of airfoils can be significant echo sources. The characteristics of some common targets and target features are discussed in Sec. 11.2.

The radar cross sections of simple bodies can be computed exactly by a solution of the wave equation in a coordinate system for which a constant coordinate coincides with the surface of the body. The exact solution requires that the electric and magnetic fields just inside and just outside the surface satisfy certain conditions that depend on the electromagnetic properties of the material of which the body is made.

While these solutions constitute interesting academic exercises and can, with some study, reveal the nature of the scattering mechanisms that come into play, there are no known tactical targets that fit the solutions. Thus, exact solutions of

the wave equation are, at best, guidelines for gauging other (approximate) methods of computing scattered fields.

An alternative approach is the solution of the integral equations governing the distribution of induced fields on target surfaces. The most useful approach at solution is known as the *method of moments*, in which the integral equations are reduced to a system of linear homogeneous equations. The attraction of the method is that the surface profile of the body is unrestricted, allowing the computation of the scattering from truly tactical objects. Another is that ordinary methods of solution (matrix inversion and gaussian elimination, for example) may be employed to effect a solution. The method is limited by computer memory and execution time, however, to objects a few dozen wavelengths in size at best.

Alternatives to these exact solutions are several approximate methods that may be applied with reasonable accuracy to electrically large target features. They include the theories of geometrical and physical optics, the geometrical and physical theories of diffraction, and the method of equivalent currents. These approximations are discussed in Sec. 11.3. Other approximate methods not discussed here are explored in detail in some of the references listed at the end of this chapter.

The practical engineer cannot rely entirely on predictions and computations and must eventually measure the echo characteristics of some targets. This may be done by using full-scale test objects or scale models thereof. Small targets often may be measured indoors, but large targets usually must be measured on an outdoor test range. The characteristics of both kinds of test facilities are described in Sec. 11.4.

Control of the echo characteristics of some targets is of vital tactical importance. There are only two practical ways of doing so: shaping and radar absorbers. Shaping is the selection or design of surface profiles so that little or no energy is reflected back toward the radar. Because target contours are difficult to change once the target has become a production item, shaping is best implemented in the concept definition stage before production decisions have been made. Radar-absorbing materials actually soak up radar energy, also reducing the energy reflected back to the radar. However, the application of such materials can be expensive, whether gauged in terms of nonrecurring engineering costs, lifetime maintenance, or reduced mission capabilities. The two methods of echo control are discussed in Sec. 11.5.

Unless otherwise noted, the time convention used in this chapter is exp $(-i\omega t)$, with the time dependence suppressed in all equations. Readers who prefer the exp $(j\omega t)$ time convention may replace i by $-j$ wherever it appears.

11.2 THE CONCEPT OF ECHO POWER

Definition of RCS. An object exposed to an electromagnetic wave disperses incident energy in all directions. This spatial distribution of energy is called *scattering*, and the object itself is often called a *scatterer*. The energy scattered back to the source of the wave (called *backscattering*) constitutes the *radar echo* of the object. The intensity of the echo is described explicitly by the radar cross section of the object, for which the abbreviation RCS has been generally recognized. Early papers on the subject called it the *echo area* or the *effective area*, terms still found occasionally in contemporary technical literature.

The formal definition of radar cross section is

$$\sigma = \lim_{R \to \infty} 4\pi R^2 \frac{|E_s|^2}{|E_0|^2} \tag{11.1}$$

where E_0 is the electric-field strength of the incident wave impinging on the target and E_s is the electric-field strength of the scattered wave at the radar. The derivation of the expression assumes that a target extracts power from an incident wave and then radiates that power uniformly in all directions. Although the vast majority of targets do *not* scatter energy uniformly in all directions, the definition assumes that they do. This permits one to calculate the scattered power density on the surface of a large sphere of radius R centered on the scattering object. R is typically taken to be the range from the radar to the target.

The symbol σ has been widely accepted as the designation for the RCS of an object, although this was not so at first.[1,2] The RCS is the projected area of a metal sphere which is large compared with the wavelength and which, if substituted for the object, would scatter identically the same power back to the radar. The RCS of all but the simplest scatterers fluctuates greatly with the orientation of the object. As such, this imaginary sphere would have to expand and contract with changing target orientation to represent the amplitude fluctuations displayed by most objects.

The limiting process in Eq. (11.1) is not always an absolute requirement. In both measurement and analysis, the radar receiver and transmitter are usually taken to be in the far field of the target (discussed in Sec. 11.4), and at that distance the scattered field E_s decays inversely with the distance R. Thus, the R^2 term in the numerator of Eq. (11.1) is canceled by an identical but implicit R^2 term in the denominator. Consequently the dependence of the RCS on R, and the need to form the limit, usually disappears.

Radar cross section is therefore a comparison of the scattered power density at the receiver with the incident power density at the target. An equally valid definition of the RCS results when the electric-field strengths in Eq. (11.1) are replaced with the incident and scattered magnetic-field strengths. It is often necessary to measure or calculate the power scattered in some other direction than back to the transmitter, a *bistatic* situation. A bistatic RCS may be defined for this case as well as for backscattering, provided it is understood that the distance R is measured from the target to the receiver. *Forward scattering* is a special case of bistatic scattering in which the bistatic angle is 180°, whence the direction of interest is along the shadow zone behind the target.

The shadow itself can be regarded as the sum of two fields of nearly equal strength but 180° out of phase. One is the incident field, and the other is the scattered field. The formation of the shadow implies that the forward scattering is large, which is indeed the case. The fields behind the target are hardly ever precisely zero, however, because some energy usually reaches the shadow zone via diffraction from the sides of the target.

While there are few two-dimensional (infinite cylindrical) objects in the physical world, analyses of the scattering from two-dimensional structures are very useful. A two-dimensional object is, by definition, a cylinder formed by the pure translation of a plane curve to plus and minus infinity along an axis perpendicular to the plane of that curve. Many scattering problems become analytically tractable when there is no field variation along the cylindrical axis, such as when the infinite structure is illuminated by a plane wave propagating at right angles to the cylinder axis.

In this case, one defines a scattering *width* instead of a scattering area,

$$\sigma_{2D} = \lim_{\rho \to \infty} 2\pi\rho \frac{V_s^{\,2}}{V_0^{\,2}} \qquad (11.2)$$

where ρ is the distance from the cylindrical body to a remove receiver, measured perpendicularly to the cylindrical axis. We have appended the subscript 2D to distinguish the scattering width of Eq. (11.2), whose dimension is length, from the scattering cross section of Eq. (11.1), whose dimension is the square of length.

By virtue of the linear properties of electromagnetic fields, the solutions of two-dimensional problems may be resolved into two cases, one each for the electric field or the magnetic field parallel to the cylindrical axis. The ratio $|V_s|/|V_0|$ thus represents either the incident and scattered electric fields or the incident and scattered magnetic fields, depending on the case at hand. These two cases are often called E and H polarizations, respectively. They are also known as TM and TE polarizations.

Practical three-dimensional problems often involve truncated segments of two-dimensional structures, such as shown in Fig. 11.1. In the practical world, those segments may be viewed at angles other than incidence perpendicular to the cylindrical axis, as implied in the solution of two-dimensional problems. The three-dimensional RCS of a truncated two-dimensional structure may be found from the approximate relationship

$$\sigma = \frac{2\ell^2 \sigma_{2D}}{\lambda} \left| \frac{\sin(k\ell \sin \tau)}{k\ell \sin \tau} \right|^2 \qquad (11.3)$$

where ℓ is the length of the truncated structure, σ_{2D} is its two-dimensional scattering width (obtained for the infinite structure), and τ is the tilt angle of the segment measured from broadside incidence. This approximation assumes that the amplitudes of the fields induced on the three-dimensional body are identically those induced on the corresponding two-dimensional structure and that the tilt angle influences only the phase of the surface fields induced on the body. The expression should not be used for large tilt angles, for which the amplitudes obtained from the two-dimensional solution no longer apply to the three-dimensional problem.
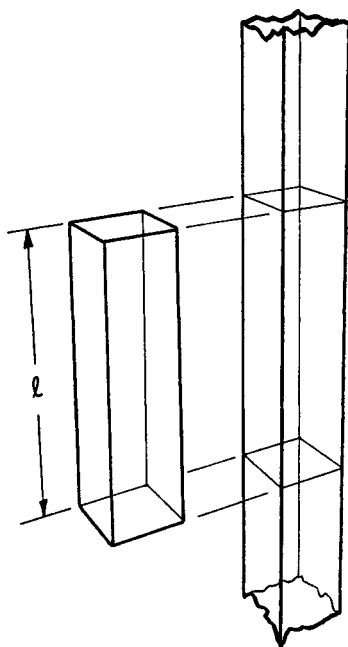

FIG. 11.1 A three-dimensional object whose profile does not vary along its length, such as the truncated rectangular cylinder on the left, is a finite chunk of an infinite (two-dimensional) structure having the same profile, such as the one on the right. Equation (11.3) relates the RCS of the two structures.

Examples of RCS Characteristics

Simple Objects. Because of its pure radial symmetry, the perfectly conducting sphere is the simplest of all three-dimensional scatterers. Despite the simplicity of its geometrical surface, however, and the invariance of its echo with orientation, the RCS of the sphere varies considerably with electrical size.

The exact solution for the scattering by a conducting sphere is known as the Mie series,[3] illustrated in Fig. 11.2.
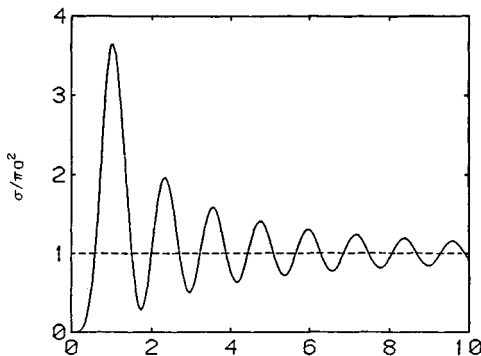

FIG. 11.2 RCS of a perfectly conducting sphere as a function of its electrical size ka.

The parameter $ka = 2\pi a/\lambda$ is the circumference of the sphere expressed in wavelengths, and the RCS is shown normalized with respect to the projected area of the sphere. The RCS rises quickly from a value of zero to a peak near $ka = 1$ and then executes a series of decaying undulations as the sphere becomes electrically larger. The undulations are due to two distinct contributions to the echo, one a *specular reflection* from the front of the sphere and the other a *creeping wave* that skirts the shadowed side. The two go in and out of phase because the difference in their electrical path lengths increases continuously with increasing ka. The undulations become weaker with increasing ka because the creeping wave loses more energy the longer the electrical path traveled around the shadowed side.

The log-log plot of Fig. 11.3 reveals the rapid rise in the RCS in the region $0 < ka < 1$, which is known as the *Rayleigh region*. Here the normalized RCS increases with the fourth power of ka, a feature shared by other electrically small or thin structures. The central region characterized by the interference between the specular and creeping-wave contributions is known as the *resonance region*. There is no clear upper boundary for this part of the curve, but a value near $ka = 10$ is generally accepted. The region $ka > 10$ is dominated by the specular return from the front of the sphere and is called the *optics region*. For spheres of these sizes the geometric optics approximation πa^2 is usually an adequate representation of the magnitude of the RCS.

The echoes of all scattering objects, and not just the perfectly conducting sphere, can be grouped according to the electrical-size characteristics of the object. The dimensions of a Rayleigh scatterer are much less than a wavelength, and the RCS is proportional to the square of the volume of the body. Resonant scatterers are generally of the order of one-half to 10 wavelengths in size, for which neither Rayleigh nor optics approximations may be very accurate. In the optics region several approximations are available for making estimates or predictions (see Sec. 11.3).
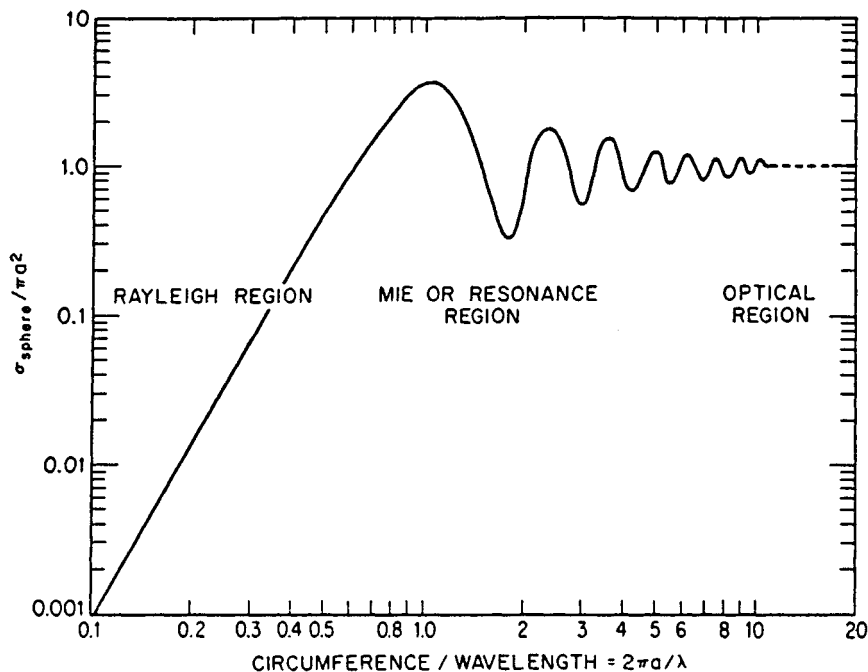
FIG. 11.3 Log-log version of the data displayed in Fig. 11.2.

The echo characteristics of permeable (dielectric) bodies can be more complicated than those of perfect conductors because energy may enter the body and suffer several internal bounces before emerging. An example is the dielectric sphere whose RCS is plotted in Fig. 11.4. Because the dielectric material is slightly lossy, as indicated by the nonzero imaginary component of the index of refraction, the RCS of the sphere decays gradually with increasing electrical size. The RCS of small dielectric bodies does not exhibit this complexity, on the other hand, because the sources of reflection are too close to each other to be resolvable by the incident wave. An example is the two-dimensional Rayleigh region RCS of a thin dielectric cylinder, plotted in Fig. 11.5. The thin dielectric cylinder has been used to model the target support lines sometimes employed in RCS measurements.[5] Note that the H-polarized echo is barely 6 dB less than that for E polarization for this particular dielectric constant.

The thin wire (a metal dipole) can have a complicated pattern, as shown in Fig. 11.6. The RCS of the wire varies with the wire length, the angle subtended by the wire and the line of sight, and on that component of the incident electric field in the plane containing the wire and the line of sight. The wire diameter has only a minor influence if it is much smaller than the wavelength. In addition to the prominent broadside lobe at the center of the pattern, there are traveling-wave lobes near the left and right sides. The traveling-wave lobes tend to disappear as the dipole becomes shorter and are closely related to those excited on traveling-wave antennas.
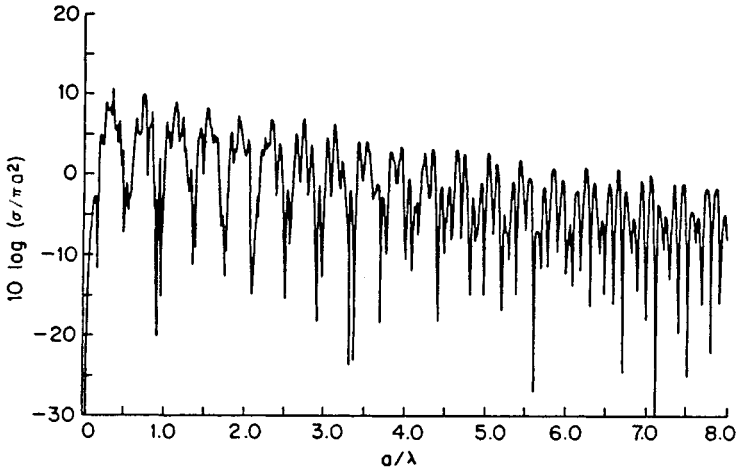
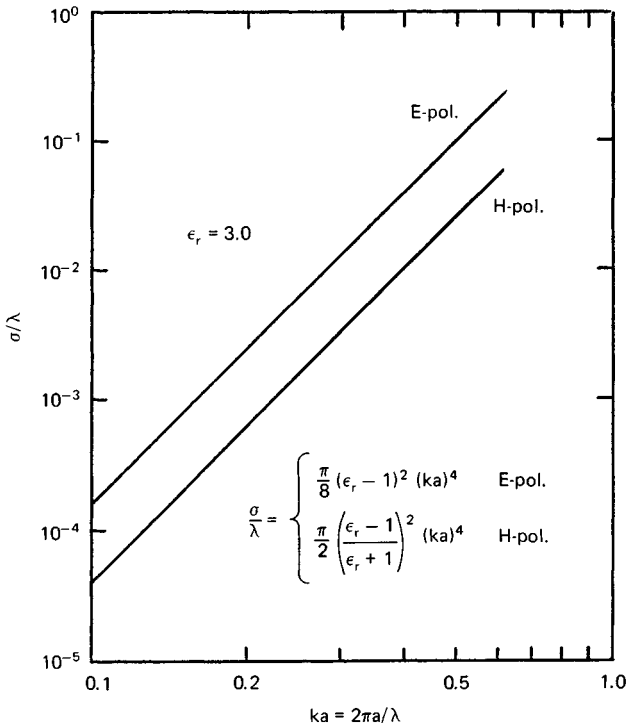**FIG. 11.4**   RCS of a lossy dielectric sphere with $n = 2.5 + i0.01$. (*Copyright 1968, IEEE.*[4])

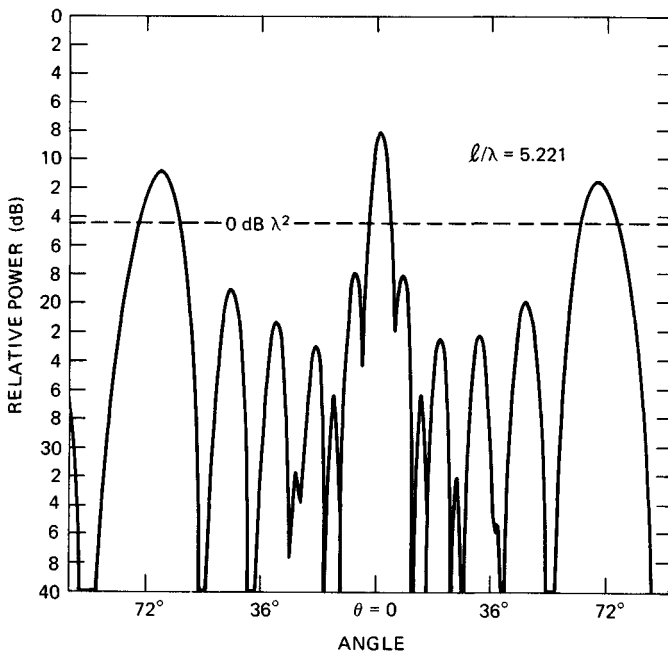**FIG. 11.5**   RCS of a slender dielectric cylinder with $\epsilon_r = 3.0$.

FIG. 11.6 Measured RCS pattern of a dipole 5.221λ long. (*Courtesy of University of Michigan Radiation Laboratory.*[6])

Figure 11.7 shows the broadside resonances of a wire dipole as a function of dipole length. The first resonance occurs when the dipole is just under a half wavelength long, and its magnitude is very nearly λ^2. Other resonances occur near odd multiples of a quarter wavelength, with plateaus of nearly constant re-
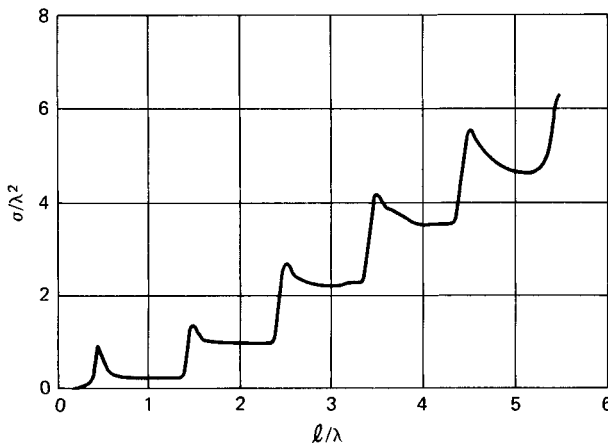

FIG. 11.7 Measured broadside returns of a thin dipole. (*Courtesy of University of Michigan Radiation Laboratory.*[6])

11.8

turn between the resonant peaks. These plateaus rise as the dipole becomes thicker, and the resonances eventually disappear.

Bodies considerably thicker than the thin wire also support surface traveling waves that radiate power in the backward direction. An example is the ogive, a spindle-shaped object formed by rotating an arc of a circle about its chord. Figure 11.8 is the RCS pattern of a 39-wavelength 15° half-angle ogive recorded for horizontal polarization (incident electric field in the plane of the ogive axis and the line of sight). The large lobe at the right side of the pattern is a specular echo in the broadside sector, and the sequence of peaks at the left side is the contribution of the surface traveling wave near end-on incidence. Note that the RCS is extremely small (not measurable in this case) at precisely end-on incidence. Theoretical predictions in the end-on region closely match the measured pattern for this particular body.
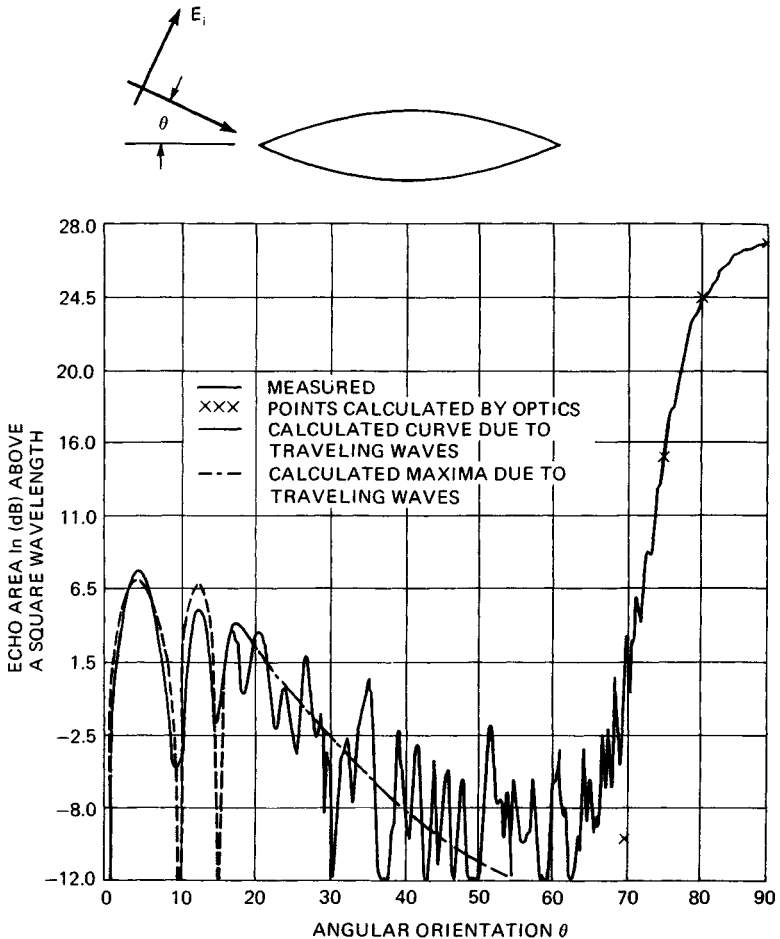

FIG. 11.8 Measured RCS pattern of a 39-wavelength 15° half-angle metal ogive. (*Copyright 1958, IEEE.*[7])

The dominant scattering mechanisms for the right circular conducting cone are the tip and the base. The return from the tip is very small in the nose-on region, and the RCS pattern is dominated by the echo from the base. Figures 11.9 and 11.10 are patterns of the RCS of a 15° (half-angle) cone with a base circumference of 12.575λ. Both patterns were measured as the cone was rotated about a vertical axis parallel to the base of the cone. The transmitted and received electric polarization was in the plane swept out by the cone axis (horizontal polarization) for Fig. 11.9 and was perpendicular to that plane (vertical polarization) for Fig. 11.10.

Nose-on incidence lies at the center of the patterns, and the sharp peaks near the sides are the specular returns from the slanted sides of the cone, also called specular *flashes*. The RCS formula for singly curved surfaces given in Table 11.1 may be used to predict the amplitudes of the specular flash within a fraction of a decibel. At precisely nose-on incidence the RCS must be independent of polarization because the cone is a body of axial symmetry. This may be verified by comparing the nose-on values in the two figures. At this angle the entire ring of the base of the cone is excited, but as the aspect angle swings away from nose-
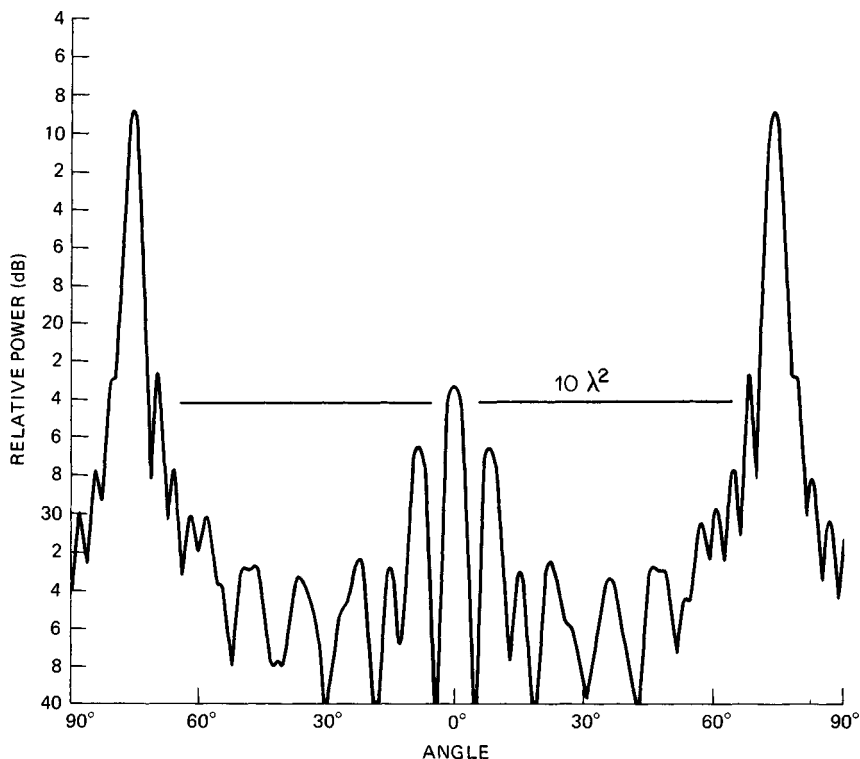

FIG. 11.9 Measured RCS of a 15° half-angle cone (horizontal polarization). The base circumference is 12.575λ. The heavy horizontal line indicates $10\lambda^2$. (*Courtesy of University of Michigan Radiation Laboratory.*[8])
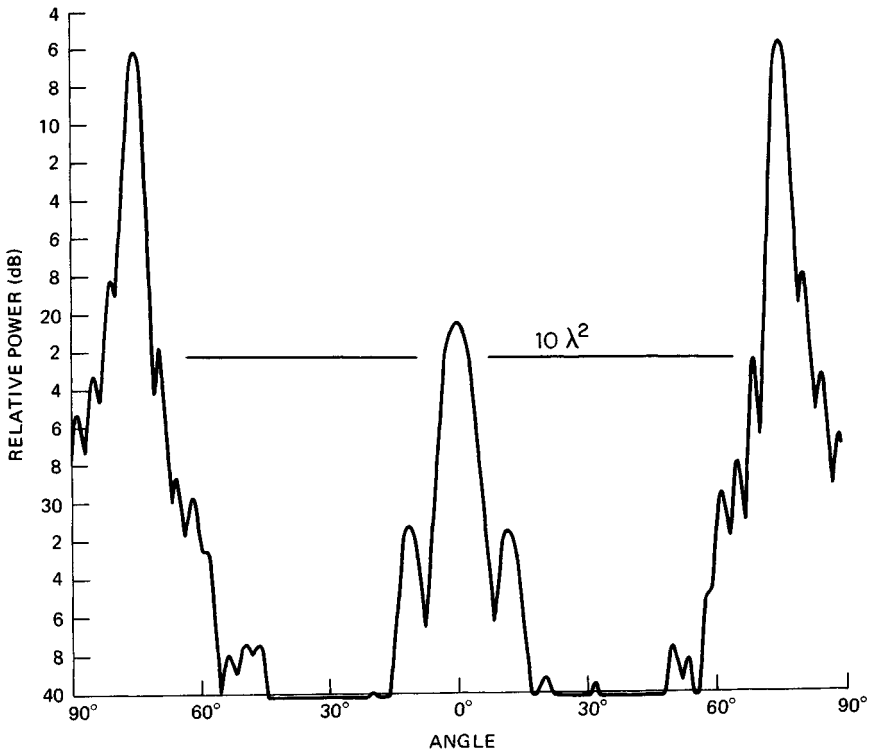
FIG. 11.10 Measured RCS of a 15° half-angle cone (vertical polarization). The base circumference is 12.575λ. The heavy horizontal line indicates 10λ². (*Courtesy of University of Michigan Radiation Laboratory.*[8])

TABLE 11.1 RCS Approximations for Simple Scattering Features

Scattering feature	Orientation (1)	Approximate RCS	
Corner reflector	Axis of symmetry along LOS	$4\pi A_{eff}^2/\lambda^2$	(2)
Flat plate	Surface perpendicular to LOS	$4\pi A^2/\lambda^2$	(3)
Singly curved surface	Surface perpendicular to LOS	$2\pi a\ell^2/\lambda$	(4)
Doubly curved surface	Surface perpendicular to LOS	$\pi a_1 a_2$	(5)
Straight edge	Edge perpendicular to LOS	ℓ^2/π	(6)
Curved edge	Edge element perpendicular to LOS	$a\lambda/2$	(7)
Cone tip	Axial incidence	$\lambda^2 \sin^4(\alpha/2)$	(8)

NOTES:
1. LOS = line of sight.
2. A_{eff} = effective area contributing to multiple internal reflections.
3. A = actual area of the plate.
4. a = mean radius of curvature; ℓ = length of slanted surface.
5. a_1, a_2 = principal radii of surface curvature in orthogonal planes.
6. ℓ = edge length.
7. a = radius of edge contour.
8. α = half angle of the cone.

on, the scattering from the base degenerates to a pair of flash points. They lie at opposite ends of a diameter across the base in the plane containing the direction of incidence and the cone axis.

The echoes from the flash points at the sides of the base weaken as the aspect angle moves away from nose-on incidence, and the sidelobes seen at $+13°$ in Fig. 11.10 are actually due to an interaction between the two flash points *across the shadowed side* of the base. (The sidelobes disappear when a pad of absorber is cemented to the base.[8]) The flash point at the far side of the base disappears when the aspect angle moves outside the backward half cone, but the near flash point remains visible, and its echo decays with increasing aspect angle. Trailing-edge contributions like these are excited by that component of the incident electric field perpendicular to the edge; therefore they are stronger for horizontal incident polarization than for vertical polarization.

A flat plate also can support multiple diffraction from one side of the plate to the other, as shown in Fig. 11.11. The axis of rotation was in the plane of the plate parallel to one edge; normal incidence to the incident wave is $0°$, at the left side of each chart, with edge-on incidence at $90°$ near the right side. The specular return from the plate is the large peak at $0°$, which is predicted with quite good accuracy by the flat-plate formula given in Sec. 11.3. The edge-on return for vertical polarization is well predicted by the straight-edge formula given in Table 11.1.
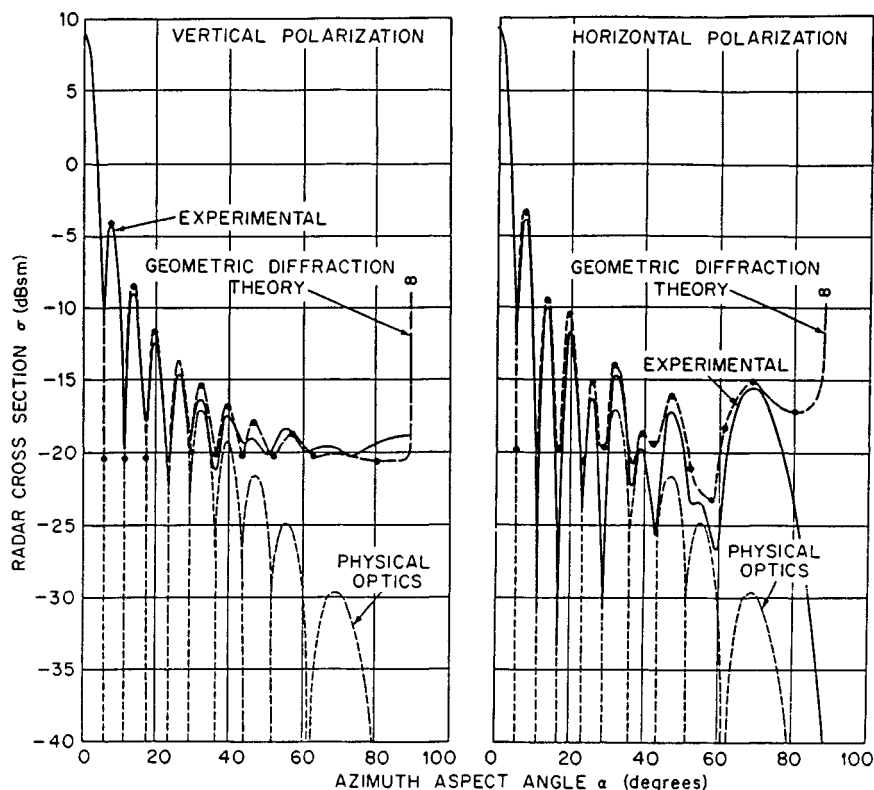

FIG. 11.11 RCS of a square flat plate 6.5 in along a side; $\lambda = 1.28$ in. (*Copyright 1966, IEEE.*[9])

These undulating patterns follow a sin x/x variation quite closely for aspect angles out to about 30°, but beyond that angle the two patterns differ by progressively wider margins. The sin x/x behavior is characteristic of a uniformly illuminated aperture, but unlike the one-way illumination function encountered in antenna work, the argument x for a flat plate includes a two-way (round-trip) illumination function. Thus, the beamwidth of the echo response of a flat plate is half the beamwidth of an antenna aperture of the same size. The prominent lobe in the horizontal pattern at 68° is a surface traveling-wave lobe closely related to the one appearing at nearly the same angle in the dipole pattern of Fig. 11.7.

In contrast to the pattern of a flat plate, the RCS pattern of a corner reflector is quite broad. This is true because the corner reflector is a reentrant structure, and no matter what its orientation (within limits, of course), internally reflected waves are directed back toward the source of the incident wave. A corner reflector is formed by two or three flat plates intersecting at right angles, and waves impinging on the first face are reflected onto the second; if there is a third face, it receives waves reflected by the first two faces. The mutual orthogonality of the faces ensures that the direction taken by waves upon final reflection is back toward the source.

The individual faces of the corner reflector may be of arbitrary shape, but the most common is an isosceles triangle for the trihedral corner; dihedral corners typically have rectangular faces. The RCS of a corner reflector seen along its axis of symmetry is identically that of a flat plate whose physical area matches the effective area of the corner reflector. The magnitude of the echo may be determined by finding the polygonal areas on each face of the corner receiving waves reflected by the other faces, and from which the final reflection is back toward the source. The effective area is determined by summing the projections of the areas of those polygons on the line of sight;[10] the RCS is then found by squaring that area, multiplying by 4π and dividing by λ^2.

Figure 11.12 is a collection of RCS patterns of a trihedral corner reflector with triangular faces. The reflector was fabricated of three triangular plywood panels, metallized to enhance their surface reflectivities. The aperture exposed to the radar was therefore an equilateral triangle, as shown in Fig. 11.13. The eight patterns in Fig. 11.12 were measured with the plane of the aperture tilted above or below the line of sight by the angle ϕ.

The broad central part of these patterns is due to a triple-bounce mechanism between the three participating faces, while the "ears" at the sides of the patterns are due to the single-bounce, flat-plate scattering from the individual faces. Along the axis of symmetry of the trihedral reflector in Fig. 11.13 ($\theta = 0°$, $\phi = 0°$), the RCS is $\pi\ell^4/3\lambda^2$, where ℓ is the length of one of the edges of the aperture. Not shown are the echo reductions obtained when the trihedral faces are angled other than at 90° from each other. The reductions resulting from changes in the angles of the corner faces depend on the size of the faces expressed in wavelengths.[11,12]

The RCS of most of the simple scattering features discussed above may be estimated by using the simple formulas listed in Table 11.1. The RCS of some complicated targets may be estimated by representing the target as a collection of features like those listed in Table 11.1, calculating the individual contributions, and then summing the contributions coherently or noncoherently. More detailed formulas are given in Sec. 11.3 that account for surface orientations not included in Table 11.1.

Complex Objects.   Objects like antennas, insects, birds, airplanes, and ships can be much more complex than those discussed above, either because of the multiplicity of scatterers on them or because of the complexity of their surface profiles and dielectric constants. Insects are examples of the latter.
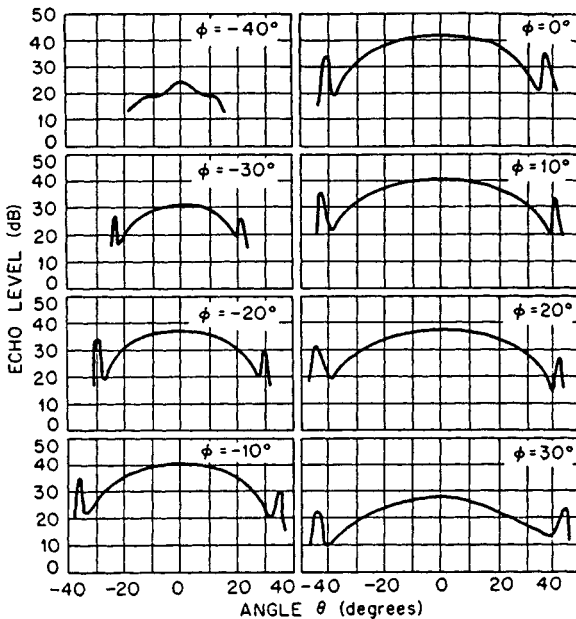
FIG. 11.12 RCS patterns of a trihedral corner reflector. Edge of aperture = 24 in; λ = 1.25 cm. (*Reprinted with permission from the* AT&T Technical Journal, *copyright 1947, AT&T.*[2])
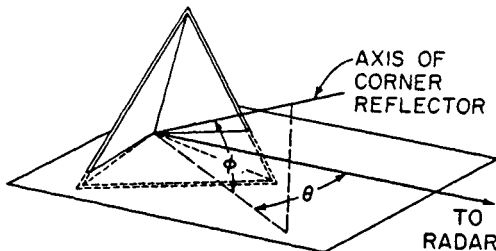

FIG. 11.13 Coordinate system for the RCS patterns in Fig. 11.12. (*Reprinted with permission from the* AT&T Technical Journal, *copyright 1947, AT&T.*[2])

Measured values for a dozen species are listed in Table 11.2. (The spider is an arachnid, not an insect, of course.) The animals were live for the measurements but had been drugged to immobilize them. Figure 11.14 shows the relationship between the RCS and the mass of an insect, with the variation of a water droplet shown for comparison. Similar comparisons have been made for both birds and insects.[15] The following values have been reported for the RCS of a man:[16]

TABLE 11.2   Measured Insect RCS at 9.4 GHz[13]

Insect	Length, mm	Width, mm	Broadside RCS, dBsm	End-on RCS, dBsm
Blue-winged locust	20	4	− 30	− 40
Armyworm moth	14	4	− 39	− 49
Alfalfa caterpillar butterfly	14	1.5	− 42	− 57
Honeybee worker	13	6	− 40	− 45
California harvester ant	13	6	− 54	− 57
Range crane fly	13	1	− 45	− 57
Green bottle fly	9	3	− 46	− 50
Twelve-spotted cucumber beetle	8	4	− 49	− 53
Convergent lady beetle	5	3	− 57	− 60
Spider (unidentified)	5	3.5	− 50	− 52

NOTE: Original values reported in square centimeters have been converted here to dBsm.
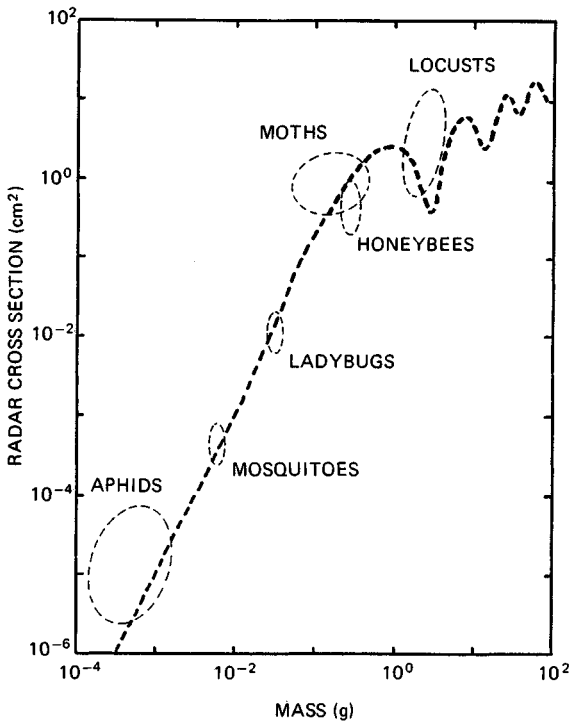

FIG. 11.14   Sample of measured RCS of insects as a function of insect mass at 9.4 GHz, based on Riley's summary. The solid trace is the calculated RCS of water droplets for comparison. (*Copyright, 1985 IEEE.*[14])

Frequency, GHz	RCS, m²
0.41	0.033–2.33
1.12	0.098–0.997
2.89	0.140–1.05
4.80	0.368–1.88
9.375	0.495–1.22

Examples of the RCS of aircraft are shown in Figs. 11.15 through 11.17. The B-26 pattern in Fig. 11.15 was measured at a wavelength of 10 cm (frequency of about 3 GHz); the polar format is useful for display purposes but is not as convenient for detailed comparisons as a rectangular format is. The RCS levels shown in the scale model Boeing 737 patterns of Fig. 11.16 are those at the measurement frequency. To obtain the corresponding full-scale values, one must add 23.5 dB (10 log 225); the full-scale frequency is one-fifteenth of the measurement frequency in this case, or 667 MHz. The patterns shown in Fig. 11.17 are medians of RCS averages taken in cells 10° square. With modern data-collecting and -recording equipment, it is feasible to plot measured results at much finer intervals than are plotted in this figure. Note that the data is relative to 1 ft²; to convert the displayed results to dBsm, one must subtract 10.3 dB (10 log 10.76 ft²/m²).
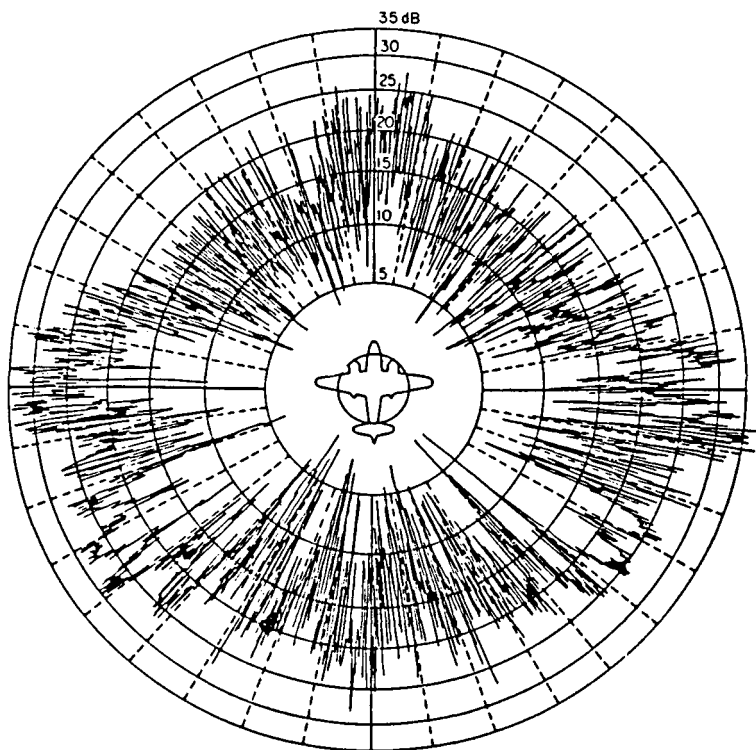

FIG. 11.15   Measured RCS pattern of a B-26 bomber at 10-cm wavelength. (*Copyright 1947, McGraw-Hill Book Company.*[17])
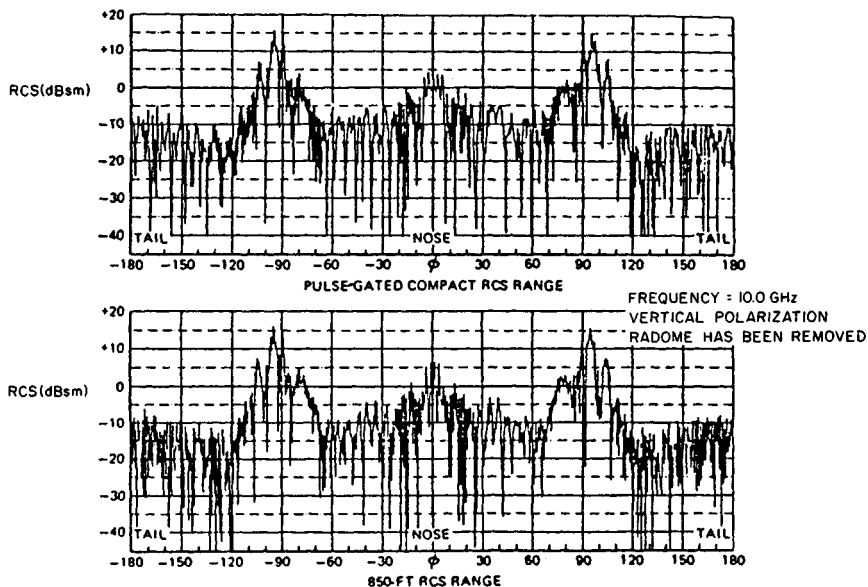
FIG. 11.16 Measured RCS of a one-fifteenth scale model Boeing 737 commercial jetliner at 10 GHz and vertical polarization. (*Copyright 1970, IEEE.*[18])

Figure 11.18 charts the RCS of a ship measured at 2.8 and 9.225 GHz at horizontal polarization. The data was collected by a shore-based radar instrumentation complex as the ship steamed in a large circle on Chesapeake Bay. The three traces in these charts are the 80, 50, and 20 percentile levels of the signals collected over aspect angle "windows" 2° wide. The patterns are not symmetrical, especially at the higher frequency. Note that the RCS can exceed 1 mi² (64.1 dBsm).

An empirical formula for the RCS of a naval ship is

$$\sigma = 52 f^{1/2} D^{3/2} \tag{11.4}$$

where f is the radar frequency in megahertz and D is the full-load displacement of the vessel in kilotons.[20,21] The relationship is based on measurements of several ships at low grazing angles and represents the average of the median RCS in the port and starboard bow, and quarter aspects, but excluding the broadside peaks. The statistics include data collected at nominal wavelengths of 3.25, 10.7, and 23 cm for ship displacements ranging from 2 to 17 kilotons.

Figure 11.19 summarizes the general RCS levels of the wide variety of targets discussed in this section, with the RCS of a metallic sphere shown as a function of its volume for comparison. The ordinate is the RCS in square meters, and the abscissa is the volume of the target in cubic feet. Because the chart is intended only to display the wide range in RCS that may be encountered in practice, the locations of targets on the chart are approximate at best. Within given classes of target the RCS may be expected to vary by as much as 20 or 30 dB, depending on frequency, aspect angle, and specific target characteristics. The reader requiring
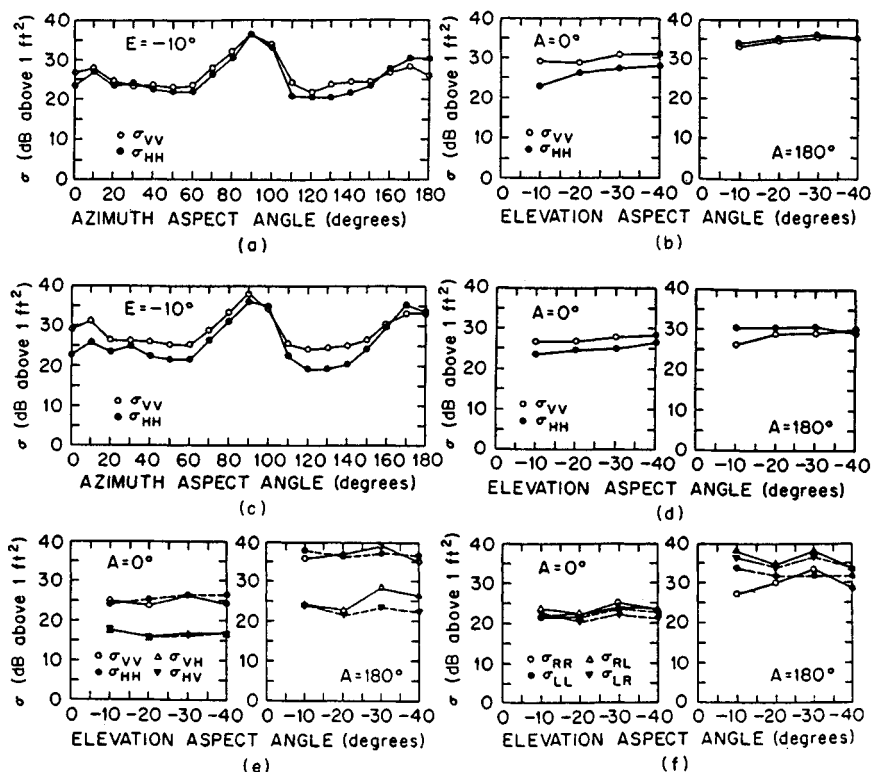
FIG. 11.17 Measured RCS of a C-54 aircraft in azimuth and elevation planes for linear and circular polarizations. Plotted values are the average RCS in a cell 10° in azimuth by 10° in elevation. Azimuth patterns *a* and *c* are for a fixed elevation angle of $-10°$. The remaining patterns are in the elevation plane for fixed nose-on or tail-on azimuths. The first and second subscripts give transmitted and received polarizations; *H* and *V* indicate horizontal and vertical polarizations, and *R* and *L* indicate right circular and left circular polarizations. (*Courtesy of I. D. Olin and F. D. Queen,*[19] *Naval Research Laboratory.*)

more explicit detail than this should consult referenced material at the end of this chapter.

11.3 RCS PREDICTION TECHNIQUES

Although the complexity and size of most scattering objects preclude the application of exact methods of radar cross-section prediction, exact solutions for simple bodies provide valuable checks for approximate methods. The exact methods are restricted to relatively simple or relatively small objects in the Rayleigh and resonant regions, while most of the approximate methods have been developed for the optics region. There are exceptions to these general limitations, of course; the exact solutions for many objects can be used for large bodies in the optics region if one uses arithmetic of sufficient precision, and many of the optics ap-
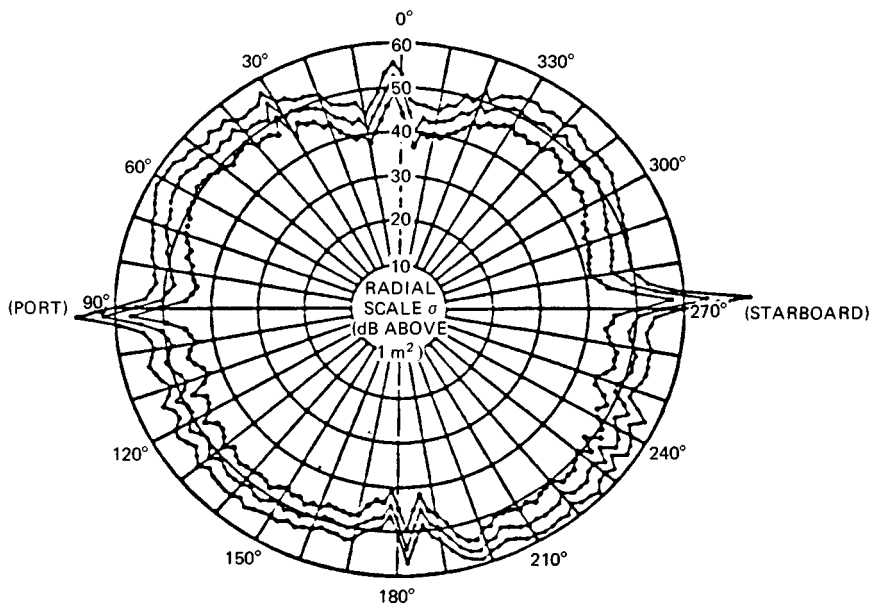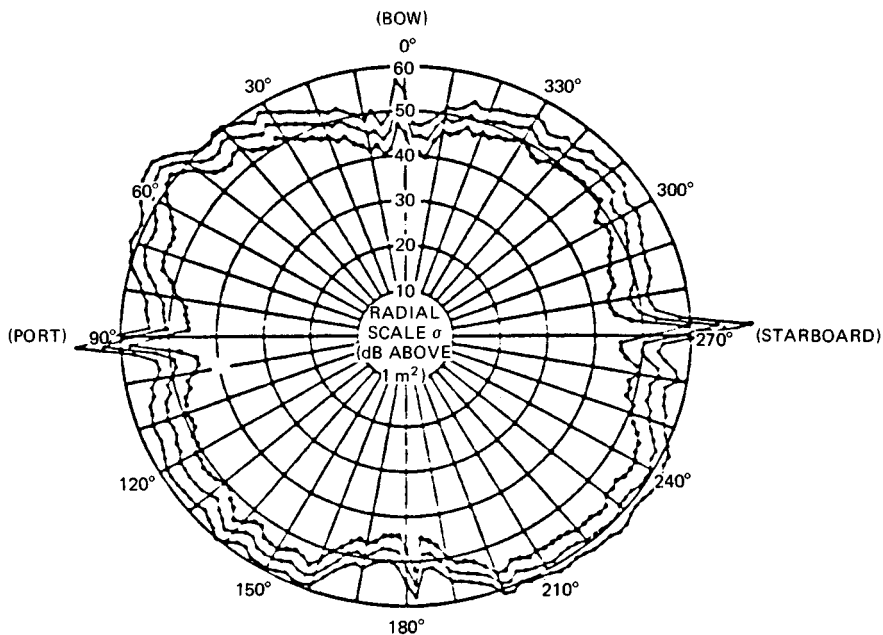
FIG. 11.18 Measured RCS of a large naval auxiliary ship for horizontal incident polarization. Upper pattern (a) is for 2.8 GHz and the lower (b) for 9.225 GHz. Shown are the 80, 50, and 20 percentile levels based on the statistics of the data over 2° aspect angle windows.
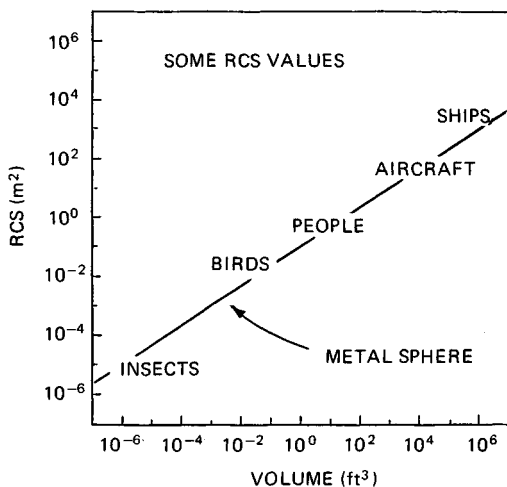
FIG. 11.19 Summary of RCS levels of targets discussed in this section. The locations of targets on the chart are general indications only.

proximations can be extended to bodies of modest electrical size in the resonance region. Low-frequency approximations developed for the Rayleigh region can extend nearly into the resonance region.

Exact Methods

Differential Equations. The exact methods are based on either the integral or differential form of Maxwell's equations. Maxwell's four differential equations constitute a succinct statement of the relationship between electric and magnetic fields produced by currents and charges and by each other.[22] The four equations may be manipulated for isotropic source-free regions to generate the wave equation

$$\nabla^2 \mathbf{F} + k^2 \mathbf{F} = 0 \tag{11.5}$$

where **F** represents either the electric field or the magnetic field. Equation (11.5) is a second-order differential equation which may be solved as a boundary-value problem when the fields on the surface of the scattering obstacle are specified. The fields are typically represented as the sum of known and unknown components (incident and scattered fields), and the boundary conditions are the known relationships that must be satisfied between the fields (both electric and magnetic) just inside and just outside the surface of the obstacle exposed to the incident wave. Those boundary conditions are particularly simple for solid conducting or dielectric objects.

The boundary conditions involve all three components of the vector fields, and the surface of the body must coincide with a coordinate of the geometrical system in which the body is described. The solution of the wave equation is most useful for those systems in which the equation is separable into ordinary differential equations in each of the variables. The scattered fields are typically expressed in terms of infinite series, the coefficients of which are to be determined in the actual solution of the problem. The solution allows the fields to be calculated at any point in space, which in RCS problems is the limit as the distance

from the obstacle becomes infinite. The product implied in Eqs. (11.1) and (11.2) is then formed from the solution of the wave equation, yielding the scattering cross section or the scattering width.

An example of a solution of the wave equation is the following infinite series for a perfectly conducting sphere:

$$\frac{\sigma}{\pi a^2} = \left| \sum_{n=1}^{\infty} \frac{(-1)^n(2n+1)}{f_n(ka)[ka\,f_{n-1}(ka) - nf_n(ka)]} \right|^2 \qquad (11.6)$$

The function $f_n(x)$ is a combination of spherical Bessel functions of order n and may be formed from the two immediately lower order functions by means of the recursion relationship

$$f_n(x) = \frac{2n-1}{x} f_{n-1}(x) - f_{n-2}(x) \qquad (11.7)$$

An efficient computational algorithm may be developed by using the two lowest orders as starting values,

$$f_0(x) = 1$$

$$f_1(x) = (1/x) - i$$

Equation (11.6) was used to compute the RCS characteristics plotted in Figs. 11.2 and 11.3. The infinite summation is truncated at the point where additional terms are negligible. The number of terms N required to compute the value of the bracketed term in Eq. (11.6) to six decimal places for $ka < 100$ is approximately

$$N = 8.53 + 1.21(ka) - 0.001(ka)^2 \qquad (11.8)$$

The constants in Eq. (11.8) are slightly different for $ka > 100$ and are lower in value for fewer decimal places in the required accuracy.

The solution of the wave equation for the infinite, perfectly conducting circular cylinder can be resolved into two cases, one each for the incident electric or magnetic field parallel to the cylinder axis. The expressions are slightly simpler than Eq. (11.6) and involve cylindrical Bessel functions of the first and second kinds.[23] Figures 11.20 and 11.21 illustrate the backscattering behavior for the two principal polarizations as a function of the electrical circumference of the cylinder.

The response for E polarization (Fig. 11.20) is much larger than geometric optics value, πa, when the cylinder is less than a fraction of a wavelength in circumference, but it approaches the geometric optics value within a few percent for cylinders larger than about 2 wavelengths in circumference. The backscattering is markedly different for H polarization (Fig. 11.21), exhibiting the same kind of undulations noted earlier in the case of the metallic sphere. These undulations are caused by creeping waves that propagate around the rear of the cylinder just as they do around a sphere. However, the peaks and nulls of the sphere and cylinder interference patterns are not perfectly aligned with each another, suggesting that the relative phase angles between the creeping waves and specular contributions are slightly different for the two geometries.

The exact expression for the RCS of the dielectric cylinder is more complicated than for the conducting cylinder, but it accounts for the fact that energy penetrates the interior of the body. Unless the cylinder material is a perfect in-
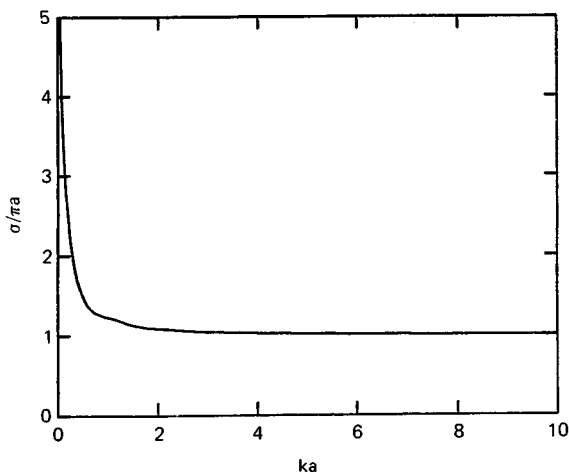
FIG. 11.20 Normalized scattering width of an infinite, perfectly conducting cylinder for E polarization (incident electric field parallel to the cylinder axis). The normalization is with respect to the geometric optics return from the cylinder.
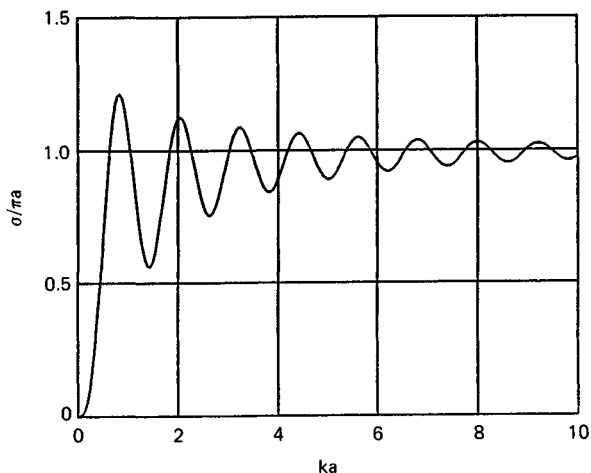

FIG. 11.21 Normalized scattering width of an infinite, perfectly conducting cylinder for H polarization (incident magnetic field parallel to the cylinder axis). The normalization is with respect to the geometric optics return from the cylinder.

sulator, its index of refraction is a complex function whose imaginary part gives rise to losses in the material. This in turn requires the computation of Bessel functions of complex argument, not an insignificant undertaking. Quite simple formulas for the scattering width may be obtained in the Rayleigh region, however, for which the cylinder diameter is much smaller than the incident wave-

length. Figure 11.5 illustrates the scattering behavior of very thin dielectric cylinders.

Integral Equations.   Maxwell's equations may also be manipulated to generate a pair of integral equations (known as the Stratton-Chu equations[24]),

$$\mathbf{E}_s = \oint \{ikZ_0(\mathbf{n} \times \mathbf{H})\psi + (\mathbf{n} \times \mathbf{E}) \times \nabla\psi + (\mathbf{n} \cdot \mathbf{E})\nabla\psi\}dS \qquad (11.9)$$

$$\mathbf{H}_s = \oint \{ - ikY_0(\mathbf{n} \times \mathbf{E})\psi + (\mathbf{n} \times \mathbf{H}) \times \nabla\psi + (\mathbf{n} \cdot \mathbf{H})\nabla\psi\}dS \quad (11.10)$$

where **n** is the unit surface normal erected at the surface patch dS and the Green's function ψ is

$$\psi = e^{ikr}/4\pi r \qquad (11.11)$$

The distance r in Eq. (11.11) is measured from the surface patch dS to the point at which the scattered fields are desired. These expressions state that if the total electric and magnetic field distributions are known over a closed surface S, the scattered fields anywhere in space may be computed by summing (integrating) those surface field distributions.

The surface field distributions may be interpreted as induced electric and magnetic currents and charges, which become unknowns to be determined in a solution. The two equations are coupled because the unknowns appear in both. Unknown quantities also appear on both sides of the equations because the induced fields include the known incident field intensity and the unknown scattered field intensity. The method of solution is known as the *method of moments* (MOM),[25] reducing the integral equations to a collection of homogeneous linear equations which may be solved by matrix techniques.

The solution of the integral equations begins with the specification of the relation between the incident and scattered fields on the surface S, as governed by the material of which the object is made. If the body is perfectly conducting or if the electric and magnetic surface fields can be related by a constant (the surface impedance boundary condition), the equations become decoupled, and only one or the other need be solved. If the body is not homogeneous, the fields must be sampled at intervals within its interior volume, complicating the solution.

Once the boundary conditions have been specified, the surface S is split into a collection of small discrete patches, as suggested in Fig. 11.22. The patches must be small enough (typically less than 0.2λ) that the unknown currents and charges on each patch are constant or at least can be described by simple functions. A weighting function may be assigned to each patch, and the problem is essentially solved when the amplitude and phase of those functions have been determined.

The point of observation is forced down to a general surface patch, whereupon the fields on the left sides of Eqs. (11.9) and (11.10) are those due to the coupling of the fields on all other patches, plus the incident fields and a "self-field." The self-field (or current or charge) is moved to the right side of the equations, leaving only the known incident field on the left side. When the process is repeated for each patch on the surface, a system of $2n$ linear homogeneous equations in $2n$ unknowns is generated. If the boundary conditions permit the decoupling of the equations, the number of unknowns may be halved (n equations in n unknowns). The coefficients of the resulting matrix involve only the electrical distances (in wavelengths) between all patches taken by pairs and the orientation of the patch surface normals. The unknown fields may be found by inverting the resulting matrix and multiplying the inverted matrix by a column matrix representing the incident field at each patch. The surface fields are then summed in integrals like Eqs. (11.9) and (11.10) to obtain the scattered field, which then may be inserted in
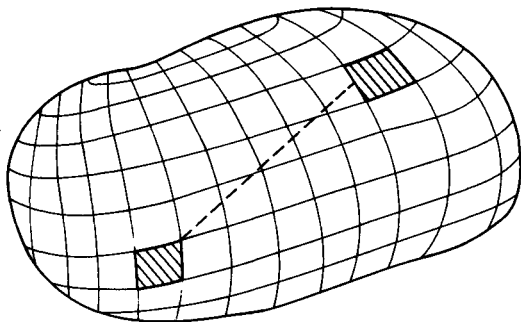
FIG. 11.22 The method of moments divides the body surface into a collection of discrete patches.

Eq. (11.1) to compute the RCS. Equation (11.2) and the two-dimensional counterparts of Eqs. (11.9) and (11.10) must be used for two-dimensional geometries, of course.

The method of moments has become a powerful tool in the prediction and analysis of electromagnetic scattering, with applications in antenna design as well as RCS prediction. The method has three limitations, however.

First, because computer memory and processing time both increase rapidly with the electrical size of the object, MOM is economically restricted to objects not much more than a few wavelengths, or perhaps a few dozen wavelengths, in size. As such, MOM is not a useful tool for predicting the RCS of, say, a jet fighter in the beam of a radar operating at 10 GHz. The second limitation is that MOM yields numbers, not formulas, and is therefore a numerical experimental tool. Trends may be established only by running a numerical experiment repeatedly for small parametric changes in the geometry or configuration of an object or in the angle of arrival or the frequency of the incident wave. Third, the solutions for some objects may contain spurious resonances that do not actually exist, thereby reducing the confidence one may have in applying the method to arbitrary structures.

Figure 11.23 traces the broadside RCS of a perfectly conducting cube computed by means of the method of moments. Spurious resonances were suppressed in the computations by forcing the normal surface component of the magnetic field to zero. The surface of the cube was divided into 384 patches (64 patches per face), which was about the limit of the central memory of the Cyber 750 computer used in the computations. It required more than 2 h for the Cyber 750 to generate the data plotted in the figure.[26]

Approximate Methods. Approximate methods for computing scattered fields are available in both the Rayleigh and the optics regions. Rayleigh region approximations may be derived by expanding the wave equation (11.5) in a power series of the wavenumber k.[27] The expansion is quasi-static for small wavenumbers (long wavelengths compared with typical body dimensions), and higher-order terms become progressively more difficult to obtain. The RCS pattern of a Rayleigh scatterer is very broad, especially if the object has similar transverse and longitudinal dimensions. The magnitude of the echo is proportional to the square of the volume of the object and varies as the fourth power of the frequency of the incident wave.[28] Because the method of moments

is well suited to the solution of Rayleigh region problems, approximate methods for predicting the RCS of electrically small objects are not presented here.

Several approximate methods have been devised for the optics region, each with its particular advantages and limitations. The most mature of the methods are *geometric optics* and *physical optics*, with later methods attacking the problem of diffraction from edges and shadow boundaries. While the general accuracy of the optics region approximations improves as the scattering obstacle becomes electrically larger, some of them give reasonably accurate results (within 1 or 2 dB) for objects as small as a wavelength or so.

The theory of geometric optics is based on the conservation of energy within a slender fictitious tube called a *ray*. The direction of propagation is along the tube, and contours of equal phase are perpendicular to it. In a lossless medium, all the energy entering the tube at one end must come out the other, but energy losses within the medium may also be accounted for. An incident wave may be rep-

FIG. 11.23 Broadside RCS of a perfectly conducting cube (s = edge length). (*Copyright 1985, IEEE.*[26])

resented as a collection of a large number of rays, and when a ray strikes a surface, part of the energy is reflected and part is transmitted across the surface. The amplitude and phase of the reflected and transmitted rays depend on the properties of the media on either side of the surface. The reflection is perfect if the surface is perfectly conducting, and no energy is transmitted across the boundary. When energy can pass through the surface, transmitted rays are bent toward the surface normal in crossing a surface into an electrically denser medium (higher index of refraction) and away from the surface normal into a less dense medium. This bending of rays is known as *refraction*.

Depending on surface curvature and body material, reflected and transmitted rays may diverge from one another or they may converge toward each other. This dependence is the basis for the design of lenses and reflectors at radar wavelengths as well as optical wavelengths. The variation of the refractive index of the water molecule with wavelength is responsible for the rainbow, the result of two refractions near the front of a spherical water droplet and a single internal reflection from the rear. Secondary and tertiary rainbows are due to double and triple internal reflections.

The reduction in intensity as the rays diverge (spread away) from the point of reflection can be calculated from the curvatures of the reflecting surface and the incident wave at the *specular point*, that point on the surface where the angle of reflection equals the angle of incidence. The principal radii of curvature of the surface are measured in two orthogonal planes at the specular point, as shown in Fig. 11.24. When the incident wave is planar and the direction of interest is back toward the source, the geometric optics RCS is simply
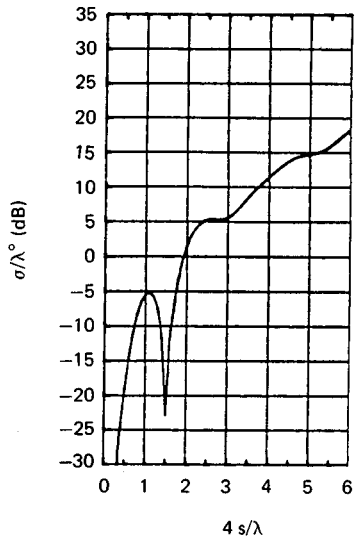
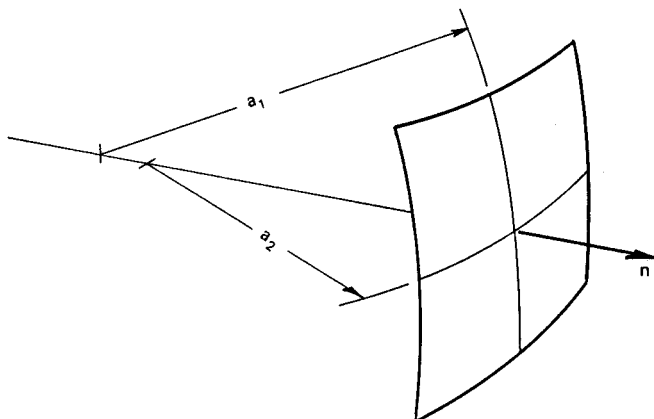$$\sigma = \pi a_1 a_2 \qquad (11.12)$$

FIG. 11.24 The geometric optics RCS of a doubly curved surface depends on the principal radii of curvature at the specular point. The specular point is that point on the surface where the surface normal points toward the radar.

where a_1 and a_2 are the radii of curvature of the body surface at the specular point.

This formula becomes exact in the optical limit of vanishing wavelength and is probably accurate to 10 or 15 percent for radii of curvature as small as 2 or 3 wavelengths. It assumes that the specular point is not close to an edge. When applied to dielectric objects, the expression should be multiplied by the square of the voltage reflection coefficient associated with the material properties of the object. Internal reflections should also be accounted for, and the phase of internally reflected rays adjusted according to the electrical path lengths traversed within the body material. The net RCS then should be computed as the coherent sum of the surface reflection plus all significant internal reflections. Equation (11.12) fails when one or both surface radii of curvature at the specular point become infinite, yielding infinite RCS, which is obviously wrong. This occurs for flat and singly curved surfaces.

The theory of physical optics (PO) is a suitable alternative for bodies with flat and singly curved surface features. The theory is based on two approximations in the application of Eqs. (11.9) and (11.10), both of which are reasonably effective approximations in a host of practical cases. The first is the *far-field approximation*, which assumes that the distance from the scattering obstacle to the point of observation is large compared with any dimension of the obstacle itself. This allows one to replace the gradient of Green's function with

$$\nabla \psi = ik\psi_o \mathbf{s} \tag{11.13}$$

$$\psi_o = e^{-ik\mathbf{r} \cdot \mathbf{s}} e^{ikR_o}/4\pi R_o \tag{11.14}$$

where $\mathbf{r}$ is the position vector of integration patch dS and $\mathbf{s}$ is a unit vector pointing from an origin in or near the object to the far-field observation point, usually

back toward the radar.[29] R_o is the distance from the origin of the object to the far-field observation point.

The second is the *tangent plane approximation*, in which the tangential field components $\mathbf{n} \times \mathbf{E}$ and $\mathbf{n} \times \mathbf{H}$ are approximated by their geometric optics values. That is, a tangent plane is passed through the surface coordinate at the patch dS, and the total surface fields are taken to be precisely those that would have existed had the surface at dS been infinite and perfectly flat. Thus the unknown fields in the integrals of Eqs. (11.9) and (11.10) may be expressed entirely in terms of the known incident field values. The problem then becomes one of evaluating one of the two integrals and substituting the result into Eq. (11.1) to obtain the RCS.

If the surface is a good conductor, the total tangential electric field is virtually zero and the total tangential magnetic field is twice the amplitude of the incident tangential magnetic field:

$$\mathbf{n} \times \mathbf{E} = 0 \tag{11.15}$$

$$\mathbf{n} \times \mathbf{H} = \begin{cases} 2\mathbf{n} \times \mathbf{H}_i & \text{illuminated surfaces} \\ 0 & \text{shaded surfaces} \end{cases} \tag{11.16}$$

Note that the tangential components of both the electric and the magnetic fields are set to zero over those parts of the surface shaded from the incident field by other body surfaces. Other approximations may be devised for nonconducting surfaces; if the incident wavelength is long enough, for example, the surface of a soap bubble or the leaf of a tree may be modeled as a thin membrane, on which neither the electric nor the magnetic fields are zero.

The integral is easy to evaluate for flat metallic plates because the phase is the only quantity within the integral that varies, and it varies linearly across the surface. The result for a rectangular plate viewed in a *principal plane* is

$$\sigma = 4\pi \left| \frac{A \cos \theta}{\lambda} \cdot \frac{\sin (k \ell \sin \theta)}{k \ell \sin \theta} \right|^2 \tag{11.17}$$

where A is the physical area of the plate, θ is the angle between its surface normal and the direction to the radar, and ℓ is the length of the plate in the principal plane containing the surface normal and the radar line of sight. A more general physical optics formula is available for the bistatic scattering of a polygonal plate with an arbitrary number of sides.[30,31]

A rectangular plate has a pair of orthogonal principal planes, and the edge length ℓ in Eq. (11.17) is that lying in the plane of measurement. If we designate w as the width of the plate in the opposite plane, the area of the plate is $A = \ell w$. To evaluate the maximum sidelobe levels of the plate RCS in the principal plane of measurement, we may replace the numerator of the sin $(x)/x$ term in Eq. (11.17) by unity. Normalizing with respect to the square of the width of the plane in the plane orthogonal to the measurement plane, we find the maximum sidelobe levels to be

$$\frac{\sigma}{w^2} = \frac{1}{\pi \tan^2 \theta} \tag{11.18}$$

Note that this result is *independent of the radar wavelength.*

The frequency independence of the principal-plane sidelobes is illustrated in Fig. 11.25. For viewing angles away from normal incidence, the plate edges are the dominant sources of echo, and the sin $(x)/x$ pattern is the result of the individual edge contributions changing phase with respect to each other as the aspect angle changes. Noting from Table 11.1 that the radar echoes of straight edges perpendicular to the line of sight are independent of frequency, the result of Eq. (11.18) is to be expected.
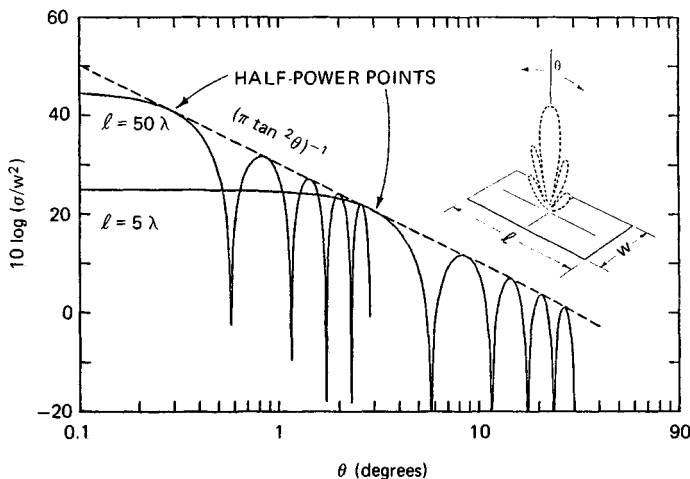

FIG. 11.25 The amplitudes of the principal-plane sidelobes of the RCS of a flat rectangular plate are independent of frequency. (*Courtesy of Walter W. Lund, Jr., The Boeing Company.*)

The physical optics formula for the RCS of a circular metallic disk is

$$\sigma = 16\pi \left| \frac{A \cos \theta}{\lambda} \cdot \frac{J_1(kd \sin \theta)}{kd \sin \theta} \right|^2 \tag{11.19}$$

where A is the physical area of the disk, d is its diameter, and $J_1(x)$ is the Bessel function of the first kind of order 1. Equations (11.17) and (11.19) both reduce to the value listed in Table 11.1 for normal incidence.

The integral is somewhat more complicated to evaluate when the surface is singly or doubly curved. An exact evaluation can be performed for a circular cylinder and a spherical cap viewed along the axis of symmetry, but not for a truncated cone or a spherical cap seen along other than the axis of symmetry. Even so, the exact evaluation for the cylinder includes fictitious contributions from the shadow boundaries at the sides of the cylinder that do not appear in a *stationary phase approximation.*[32]

The amplitude of the elemental surface patch contributions changes slowly over the surface of integration while the phase changes much more rapidly. As such, the net contribution in regions of rapid phase change is essentially zero and may be ignored. As the specular regions are approached, on the other hand, the phase variation slows down and then reverses as the specular point is crossed. This results in a nonzero specular contribution to the integral. The phase varia-

tion near the shadow boundaries is rapid; hence surface contributions there are ignored in a stationary phase evaluation, but an exact evaluation includes them because the shadow boundaries are the limits of integration. Because the actual surface field distributions do not suddenly drop to zero as the shadow boundary is crossed, as assumed by the theory, the shadow boundary contributions are spurious.[33,34] Therefore, a stationary phase approximation of the physical optics integral over closed curved surfaces tends to be more reliable than an exact evaluation.

With this in mind, the stationary phase result for a circular cylinder is

$$\sigma = ka\ell^2 \left| \frac{\sin (k\ell \sin \theta)}{k\ell \sin \theta} \right|^2 \tag{11.20}$$

where a is the radius of the cylinder, ℓ is its length, and θ is the angle off broadside incidence. Equation (11.20) includes only the contribution from the curved side of the cylinder and not its flat ends, which may be included by using the prescription of Eq. (11.19). Equation (11.20) may be used to estimate the RCS of a truncated right circular cone if the radius a is replaced by the mean radius of the cone and ℓ is replaced by the length of the slanted surface.

While the theory of physical optics offers a significant improvement over geometric optics for flat and singly curved surfaces, it suffers from other drawbacks. Although one obtains the proper result for most of the illuminated surface, the physical optics integral yields false contributions from the shadow boundaries, as noted above. Moreover, the theory shows no dependence on the polarization of the incident wave and yields different results when the receiver and the transmitter are interchanged. These effects contradict observed behavior. Finally, it errs by wider margins as the direction of observation moves farther away from the specular direction. As illustrated in Fig. 11.11, the theory is quite accurate at broadside incidence (the specular case), but the agreement between measurement and prediction becomes progressively worse as the scattering angle moves away from that direction. Keller's *geometrical theory of diffraction* (GTD) offers an improvement in both the polarization dependence and the predicted values in the wide-angle regions.[35,36]

GTD is a ray-tracing method that assigns an amplitude and phase to fields diffracted at smooth shadow boundaries and at surface discontinuities. Because the latter are much more significant in backscattering computations than the former, we focus here on edge diffraction. The theory assumes that a ray striking an edge excites a cone of diffracted rays, as in Fig. 11.26. The half angle of this *diffraction cone* is equal to the angle between the incident ray and the edge. Unless the point
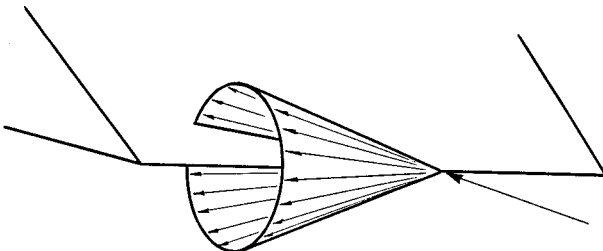

FIG. 11.26 The Keller cone of diffracted rays.

of observation lies on the diffraction cone, no value is assigned the diffracted field. The scattering direction in backscattering problems is the reverse of the direction of incidence, whence the diffraction cone becomes a disk, and the scattering edge element is perpendicular to the line of sight.

The amplitude of the diffracted field is given by the product of a *diffraction coefficient* and a *divergence factor*, and the phase depends on the phase of the edge excitation and on the distance between the observation point and the diffracting edge element. Two cases are recognized, depending whether the incident field is polarized parallel or perpendicular to the edge.

The diffracted field is given by the formula

$$E_d = \frac{\Gamma e^{iks} e^{i\pi/4}}{\sqrt{2\pi ks} \ \sin \beta} (X \mp Y) \tag{11.21}$$

where Γ is a divergence factor, X and Y are diffraction coefficients, β is the angle between the incident ray and the edge, and s is the distance to the observation point from the point of diffraction. The difference of the two diffraction coefficients is used when the incident electric field is parallel to the edge (TM polarization) and the sum when the incident magnetic field is parallel to the edge (TE polarization).

The divergence factor accounts for the decay in amplitude as the rays spread away from the edge element and includes the effects of the radius of the edge if it is curved, as at the end of a truncated cylinder, and the radius of curvature of the incident phase front.[37] The divergence factor for a two-dimensional edge (of infinite length) illuminated by a plane wave is $\Gamma = 1/s$. The diffraction coefficients are

$$X = \frac{\sin (\pi/n)/n}{\cos (\pi/n) - \cos [(\phi_i - \phi_s)/n]} \tag{11.22}$$

$$Y = \frac{\sin (\pi/n)/n}{\cos (\pi/n) - \cos [(\phi_i + \phi_s)/n]} \tag{11.23}$$

where ϕ_i and ϕ_s are the angles of the planes of incidence and scattering, as measured from one face of the wedge, and n is the exterior wedge angle normalized with respect to π; see Fig. 11.27. The three-dimensional result for an edge of finite length ℓ may be obtained by inserting Eqs. (11.22) and (11.23) in Eq. (11.21), using Eq. (11.21) for V_s/V_0 in Eq. (11.2), and then inserting Eq. (11.2) in Eq. (11.3).

Figures 11.28 and 11.29 compare measured and GTD-predicted RCS patterns of a right circular cone frustum. The theory replicates most of the pattern features for both polarizations but fails in three different aspect angle regions. These aspects are the specular directions of the flat surfaces at either end of the frustum (0 and 180° on the charts) and near the specular flash from the slanted side at 80°. The failure is due to a singularity in the diffraction coefficient Y along the reflection boundary, and a similar singularity occurs in the diffraction coefficient X along the shadow boundary, a situation encountered in forward scattering.

The singularities are overcome in the *physical theory of diffraction* (PTD) formulated by P. Ia. Ufimtsev.[39,40] (Although these publications may be difficult to find, we cite them here for completeness.) Like Keller, Ufimtsev relied on the (exact) canonical solution of the two-dimensional wedge problem, but he distin-
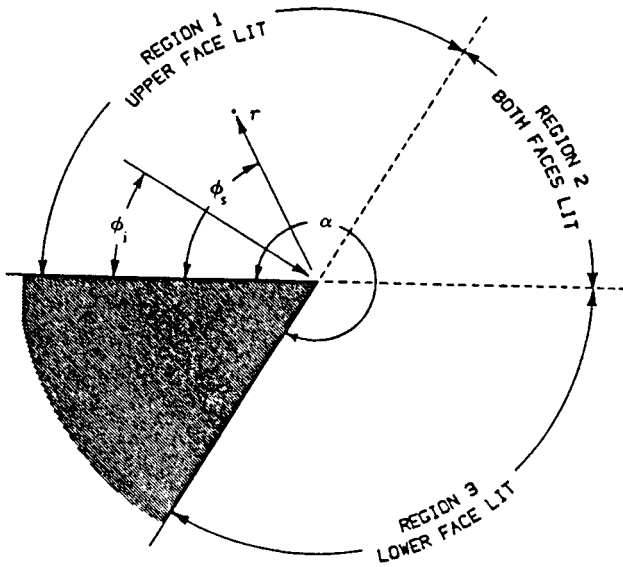
FIG. 11.27 Angles of incidence and scattering for wedge geometry.

guished between "uniform" and "nonuniform" induced surface currents. The uniform currents are the surface currents assumed in the theory of physical optics, and the nonuniform currents are associated with the edge itself (filamentary currents). The PTD result for two-dimensional problems may be represented as a linear combination of TM and TE polarizations,

$$E_s = E_0 f \frac{e^{ik\rho} e^{i\pi/4}}{\sqrt{2\pi k\rho}} \tag{11.24}$$

$$H_s = H_0 g \frac{e^{ik\rho} e^{i\pi/4}}{\sqrt{2\pi k\rho}} \tag{11.25}$$

where ρ is the distance to the far-field observation point and f and g are

$$f = \begin{cases} (X - Y) - (X_1 - Y_1) & 0 \le f_i < a\ 2\ p \\ (X - Y) - (X_1 - Y_1) - (X_2 - Y_2) & \alpha - \pi \quad \phi_i \le p \\ (X - Y) - (X_2 - Y_2) & \pi \quad \phi_i \le a \end{cases} \tag{11.26}$$

$$g = \begin{cases} (X + Y) - (X_1 + Y_1) & 0 \le f_i \le a\ 2\ p \\ (X + Y) - (X_1 + Y_1) - (X_2 + Y_2) & \alpha - \pi \quad \phi_i \le p \\ (X + Y) - (X_2 + Y_2) & \pi \quad \phi_i \le a \end{cases} \tag{11.27}$$

The subscripted coefficients are known as the *physical optics diffraction coefficients*,
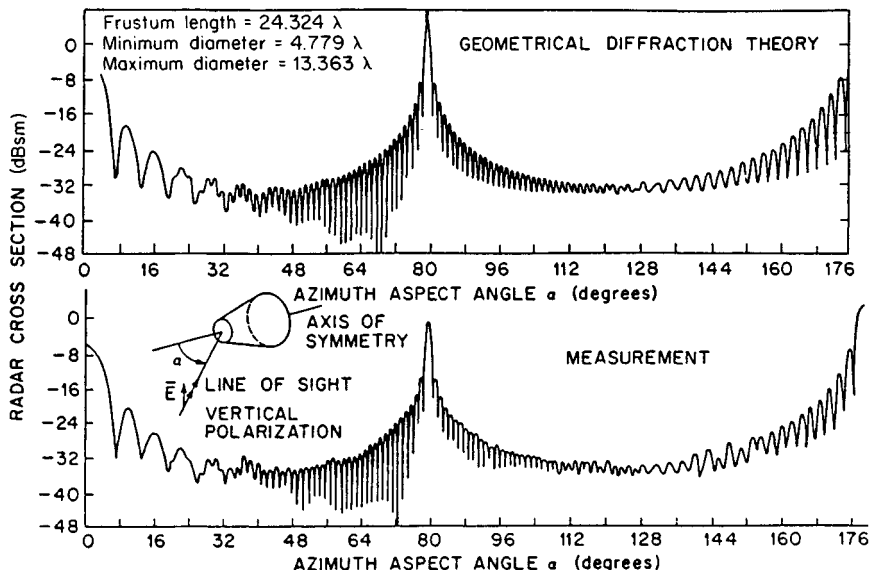
$$X_1 = -\tan\left[(\phi_s - \phi_i)/2\right] \tag{11.28}$$

FIG. 11.28   RCS of a cone frustum, vertical polarization. (*Copyright 1966, IEEE.*[38])

$$Y_1 = -\tan\left[(\phi_s + \phi_i)/2\right] \qquad (11.29)$$

$$X_2 = \tan\left[(\phi_s - \phi_i)/2\right] \qquad (11.30)$$

$$Y_2 = -\tan\left[\alpha - (\phi_s + \phi_i)/2\right] \qquad (11.31)$$

Because the PO diffraction coefficients depend on whether the upper face, the lower face, or both faces of the wedge are illuminated by the incident wave, the diffraction coefficients are combined differently in the three recognizable sectors defined in Eqs. (11.26) and (11.27). And because surface terms have been suppressed explicitly by the subtraction of the PO coefficients, the effects of surface currents (as distinguished from filamentary edge currents) must be accounted for independently. Those surface terms may be obtained, for example, by using geometrical optics or, paradoxically, the theory of physical optics after the edge terms themselves have been computed.

GTD and PTD are both based on the exact solution of the two-dimensional wedge problem, for which the directions of incidence and scattering are perpendicular to the edge. When extended to the case of oblique incidence, the direction of observation must lie along a generator of the Keller cone depicted in Fig. 11.26. If the edge is straight and of finite length, as in the three-dimensional world, Eq. (11.3) provides an approximation of the RCS. If the edge is curved, it may be regarded as a collection of infinitesimally short segments butted together, and the scattered fields may be computed via an integration of incremental fields diffracted by each element of the edge. This is the concept introduced by Mitzner,[41] and the summation of the fields diffracted by the edge elements implies an integral around the edge contour. (Although Mitzner's most significant results are embedded in a government document of limited distribution, we include this source in our references because of its significance.)

However, Mitzner sought the fields scattered in arbitrary directions, not just those along the local Keller cones, and for this purpose he developed his concept
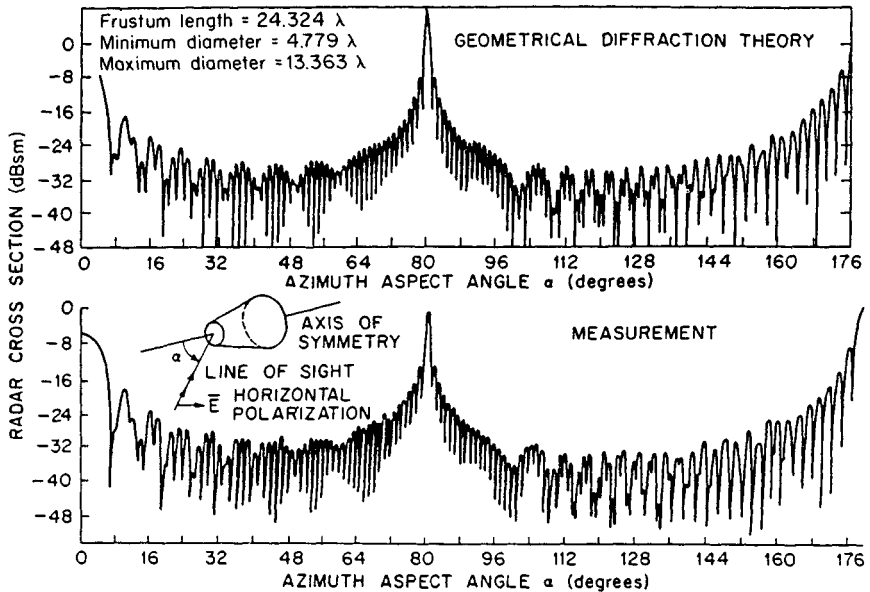
FIG. 11.29 RCS of a cone frustum, horizontal polarization. (*Copyright 1966, IEEE.*[38])

of the *incremental length diffraction coefficient*. Extending the example provided by Ufimtsev, he devised a set of diffraction coefficients for arbitrary directions of incidence and scattering. Not unexpectedly, those coefficients are more complicated than the X's and Y's appearing in Eqs. (11.22) and (11.23), and (11.28) through (11.31).[30,42]

Mitzner expressed his result as the diffracted electric-field components parallel and perpendicular to the plane of scattering in terms of the components of the incident electric field parallel and perpendicular to the plane of incidence. As such, the diffraction coefficients may be expressed as three separate pairs representing parallel-parallel, perpendicular-perpendicular, and parallel-perpendicular (or perpendicular-parallel) combinations. One member of each pair is due to the total surface current on the diffracting edge (including the assumed filamentary edge currents), and the other is due to the uniform physical optics currents. Mitzner subtracted one member of each pair from the other, thereby retaining the contributions from the filamentary currents alone.

The results have identically the form of Ufimtsev's expressions, in which the PO coefficients are subtracted from the non-PO coefficients. Thus, Mitzner's expression for the scattered field contains only the contributions from the filamentary edge currents. In applying his theory to scattering objects, therefore, the contributions of nonfilamentary induced surface currents must be accounted for separately, just as in Ufimtsev's physical theory of diffraction. When the directions of incidence and scattering become perpendicular to an edge, the perpendicular-parallel terms disappear and Mitzner's diffraction coefficients then reduce identically to Ufimtsev's.

Undertaking what he called a more rigorous evaluation of the fields induced on a wedge, Michaeli duplicated Mitzner's result for the total surface currents,

confirming Mitzner's prior development, but he did not explicitly remove the PO surface-current contributions.[43] Thus, like Keller's X and Y, Michaeli's diffraction coefficients become singular in the transition regions of the reflection and shadow directions. Michaeli later investigated the removal of the singularities, the cleverest of which was the use of a skewed coordinate system along the wedge surfaces.[44,45]

While these methods of evaluating the fields scattered by edge elements may be applicable to smooth unbounded edges, they do not account for the discontinuities at corners where the edges turn abruptly in other directions. An attack on the problem has been suggested by Sikta et al.[46]

When applying these approximate high-frequency methods of estimating the fields scattered by complex objects, it is necessary to represent the object as a collection of surfaces having relatively simple mathematical descriptions. The actual surface profiles may be approximated by segments that have conveniently simple mathematical descriptions, such as flat plates, truncated spheroids, and truncated conic sections. The total RCS may be formed by summing the field contributions of the individual segments using the methods described above or whatever other tools are available. It is important to sum the field strengths of the individual contributions, complete with phase relationships, before squaring to obtain the total RCS as given by Eq. (11.1). This is tantamount to forming the coherent sum

$$\sigma = |\sum_p \sqrt{\sigma_p} e^{i\phi_p}|^2 \tag{11.32}$$

where σ_p is the RCS of the pth contributor and ϕ_p is its relative phase angle, accounting for the two-way propagation of energy from the radar to the scattering feature and back again. If all phase angles are equally likely, one may form instead the noncoherent sum

$$\sigma = \sum_p \sigma_p \tag{11.33}$$

The noncoherent RCS is meaningful only if a change in the aspect angle or a sweep in the instantaneous radar frequency does indeed result in a uniform distribution of phase angles. It is the average RCS formed over a time interval long enough to ensure the equal likelihood of all phase angles.

11.4 RCS MEASUREMENT TECHNIQUES

RCS measurements may be required for any of several reasons, ranging from scientific inquiry to verification of compliance with product specifications. There are no formal standards governing intrumentation and measurement methods, but informal standards of good measurement practice have been recognized for decades. Depending on the size of the test object, the frequencies to be used, and other test requirements, measurements may be made in indoor test facilities or on outdoor ranges. Because one is seldom interested in the RCS of an object for only one aspect angle, all static test ranges use turntables or rotators to vary the target aspect angle. Although the purpose of testing often governs how the measure-